China Ocean Eng., 2023, Vol. 37, No. 6, P. 962–974
DOI: https://doi.org/10.1007/s13344-023-0080-9, ISSN 0890-5487
http://www.chinaoceanengin.cn/ E-mail: coe@nhri.cn

Investigations on Fluid Resonance Within A Narrow Gap Formed by Two Fixed Bodies with Varying Breadth Ratios

GONG Shu-kai[a], GAO Jun-liang[a, b, *], MAO Hong-fei[c, d]

[a] School of Naval Architecture and Ocean Engineering, Jiangsu University of Science and Technology, Zhenjiang 212100, China

[b] State Key Laboratory of Hydraulic Engineering Intelligent Construction and Operation, Tianjin University, Tianjin 300350, China

[c] College of Ocean Engineering and Energy, Guangdong Ocean University, Zhanjiang 524000, China

[d] Guangdong Provincial Key Laboratory of Intelligent Equipment for South China Sea Marine Ranching, Guangdong Ocean University, Zhanjiang 524088, China

Received June 23, 2023; revised November 8, 2023; accepted November 20, 2023

Abstract

The resonant motion of the fluid inside a narrow gap between two fixed boxes induced by incident regular waves with various wave heights is investigated by adopting a two-dimensional numerical wave flume based on an open-sourced CFD package, OpenFOAM. The two boxes have identical draft and height, but the upstream box has a variable breadth. This article focuses on the influences of the breadth ratio, defined as the ratio of the breadth of the upstream box to that of the downstream box, on the following three aspects of hydrodynamic characteristics of gap resonance: (1) the wave height amplifications inside the gap, and in front and at the rear of the structure system, (2) the reflection, transmission, and energy loss coefficients of the structure system, and (3) the response and damping time of the fluid resonance. It is found that the fluid resonant frequency, the amplification factor of the resonant wave height inside the gap and the maximum energy loss coefficient of the structure system are shown to gradually decrease with the increase of the breadth ratio. The response time of gap resonance is shown to first increase and then decrease with the breadth ratio overall, regardless of the incident wave height, and the configuration that the two boxes have the same breadth would bring the largest response time of gap resonance.

Key words: gap resonance, wave amplification, varying breadth ratios, OpenFOAM

Citation: Gong, S.K., Gao, J.L., Mao, H.F., 2023. Investigations on fluid resonance within a narrow gap formed by two fixed bodies with varying breadth ratios. China Ocean Eng., 37(6): 962–974, doi: https://doi.org/10.1007/s13344-023-0080-9

1 Introduction

In the past few decades, the fluid resonance phenomenon occurring inside narrow gaps formed between marine structures (also termed as "gap resonance") has attracted increasing attention. When the incident wave frequency is equal to or very close to the resonant frequency of the fluid within a narrow gap, the severe oscillation of the free water surface inside the gap may generate abnormally large wave loads acting on marine structures and excessive motions of the structure, ultimately posing a threat to operation safety (Liang et al., 2022; Zou et al., 2023). Hence, in order to determine a technical solution that can minimize the downtime of the offshore facility, it is crucial to further enhance the understanding of such phenomenon.

In the initial stage of gap resonance research, the classical potential flow theory was normally used for both theoretical analyses and numerical simulations. Nevertheless, owing to the neglect of the fluid viscosity in the classical potential flow theory, it significantly overestimates the wave heights within narrow gaps and the wave loads acting on marine structures (e.g., Miao et al., 2001; Molin, 2001). To overcome this issue, some special techniques have been proposed to add the so-called "artificial viscosity" into the classical potential flow theory, such as incorporating artificial damping at and/or underneath the free water surface (e.g., Ekerhovd et al., 2021; Liang et al., 2021; Ning et al., 2015a; Shivaji and Sen, 2016; Wang et al., 2022). To verify existing analytical and numerical models and to better understand the

Foundation item: This research is financially supported by the National Natural Science Foundation of China (Grant Nos. 52371277 and 52001071), the State Key Laboratory of Hydraulic Engineering Intelligent Construction and Operation (Tianjin University) (Grant No. HESS-2323), the Postgraduate Research & Practice Innovation Program of Jiangsu Province (Grant No. KYCX23_3902), and the Guangdong Basic and Applied Basic Research Foundation (Grant No.: 2023A1515010890).

*Corresponding author. E-mail: gaojunliang880917@163.com

relevant hydrodynamic features, a few laboratory experiments were also conducted in physical wave flumes to simulate the gap resonance phenomena (e.g., Saitoh et al., 2006; Song et al., 2021; Tan et al., 2014; Zhang et al., 2022; Zhao et al., 2017).

In the past ten or more years, due to the rapid development of computer science and technology, the Computational Fluid Dynamics (CFD) based numerical models have been increasingly utilized to study various wave-structure interaction phenomena including gap resonance (e.g., Gao et al., 2023a, 2023b; Xie et al., 2023; Li et al., 2024). The CFD models used in previous literatures are mainly classified into two categories, namely, mesh-based models and mesh-free ones. Among various mesh-based models, the open-sourced package OpenFOAM and the commercial software Star-CCM+ are the most widely used. For the mesh-free models, hitherto, the SPH (Smoothed Particles Hydrodynamics) model and the IMLPG_R (Improved Meshless Local Petrov-Galerkin method based on Rankine source function) model have been utilized (Meringolo et al., 2018; Vineesh and Sriram, 2021, 2023). Because of the proper consideration of the fluid viscosity, these CFD-based numerical models were found to be accurate in reproducing existing experimental data. Heretofore, the CFD-based numerical studies have considered the gap resonance phenomenon formed between not only fixed marine structures (e.g., Ding et al., 2022b; Gao et al., 2019a, 2019b, 2020b; Jiang et al., 2020, 2021; Liu et al., 2022; Yin et al., 2022, 2023) but also marine structures with one or more degrees of freedom (e.g., Ding et al., 2022a; Gao et al., 2023c, 2022a; He et al., 2022; Vineesh and Sriram, 2023).

Although numerous investigations have been conducted on gap resonance, most of them have only focused on the fluid resonance inside narrow gaps formed between marine structures with identical breadth and draft (e.g., Chen et al., 2021; Feng et al., 2017; Gao et al., 2021, 2022b; He et al., 2021a, 2021b; Jin et al., 2017; Li, 2019; Ning et al., 2015b; Tan et al., 2020; Wang et al., 2018, 2022; Zou et al., 2023). In practical operations, different marine structures, such as the FLNG (Floating Liquefied Natural Gas) production system and LNGC (Liquefied Natural Gas Carrier), typically have different breadths and drafts (Zhao et al., 2018).

However, to the best of the authors' knowledge, the investigations on the effects of different breadth ratios and/or draft ratios on gap resonance are still relatively limited. Based on the fully nonlinear potential flow theory, the fluid resonance between two barges with different relative breadths and drafts were numerically investigated by Li and Zhang (2016), and it was found that the barge draft ratio has a strong effect on the resonance frequency but the barge breadth ratio has minor effects on the latter. Subsequently, the gap resonance between two floating bodies with various breadth ratios under wave actions was studied by Liu (2017) experimentally and numerically. It was found that when the breadth of one of the two floating bodies remains constant while increasing the breadth of the other, the resonant frequency of the fluid inside the gap decreases. Meanwhile, Tan et al. (2017) adopted both a modified potential flow model and a viscous RNG turbulent model to investigate the influences of the breadth ratio on gap resonance, and have found that the breadth ratio has a significant nonlinear influence on both the resonant wave amplitude and resonant frequency.

From the above literature review, it can be seen that there is currently limited research on the effect of the breadth ratio on the gap resonance characteristics, and the research conclusions drawn are even inconsistent. Given these reasons, this article continues to focus on investigating the influences of the breadth ratio on gap resonance. Specifically, the effects of the breadth ratio on the following three aspects of hydrodynamic characteristics of gap resonance will be investigated in detail: (1) wave height amplifications near the marine structure system (including inside the narrow gap and in the vicinity of the structure system, (2) the reflection, transmission, and energy loss coefficients of the structure system, and (3) the response and damping time of the fluid resonance.

The article continues with the details of the numerical model in Section 2. The numerical wave flume adopted is described in Section 3. These are followed by the simulation results and discussion in Section 4. The article ends in Section 5 with some concluding remarks.

2 Description of the numerical model

Because significant wave energy dissipation brought about by the viscosity of real fluids during gap resonance has been observed in previous investigations (e.g., Gao et al., 2019a; Jiang et al., 2021; Tan et al., 2021), a viscous flow solver is required to accurately consider this factor. Based on an open-sourced and widely-used CFD package, OpenFOAM (version 3.0.1), a numerical wave flume for viscous fluid flows is established in this article. A third-party toolbox "waves2Foam" developed by Jacobsen et al. (2012) and a built-in two-phase flow solver "interFoam" are adopted to generate/absorb waves and simulate the interactions between incident waves and marine structures, respectively.

In the waves2Foam toolbox, the so-called "relaxation zone" technique is adopted to generate and absorb waves. Within the relaxation zone, the following functions are applied:

$$\alpha_{\mathrm{R}}(\beta_{\mathrm{R}}) = 1 - \frac{\exp\left(\beta_{\mathrm{R}}^{3.5}\right) - 1}{\exp(1) - 1}; \tag{1}$$

$$\psi_{\mathrm{R}} = \alpha_{\mathrm{R}}\psi_{\mathrm{R}}^{\mathrm{computed}} + (1 - \alpha_{\mathrm{R}})\psi_{\mathrm{R}}^{\mathrm{target}}, \tag{2}$$

where ψ_{R} is either the velocity or the volume fraction of water. The definition of β_{R} is such that α_{R} is always 1 at the interface between the non-relaxed fluid domain and the

relaxation zone, and $\beta_R \in [0, 1]$. The superscripts of "computed" and "target" represent the velocities that calculated in the computational domain and that evaluated or assigned from the chosen wave model, respectively. In the outlet relaxation zone, the target velocity is set to zero. The interFoam solver solves the incompressible Navier–Stokes equations to describe the motion of the fluid continuum. The volume of fluid (VOF) method has been used to track the interface between water and air. More detailed descriptions on the interFoam solver and the VOF method can be found in Chen et al. (2014) and Gao et al. (2021).

3 Numerical wave flume (NWF)

3.1 Setups of the NWF

Fig. 1 presents the two-dimensional NWF utilized in the present study. A Cartesian coordinate system is defined as follows. The origin, *o*, is located at the left inlet boundary and on the still water level (SWL), the positive *x*-axial direction is in line with the wave propagation direction, and the positive *z*-axial direction is in the upward direction. The *y*-axis is perpendicular to the *oxz* plane and is not shown in the figure. The length and the height of the NWF are 18.5 m and 0.9 m, respectively. Two stationary boxes (i.e., Boxes A and B) are deployed at the middle of the NWF. There exists a narrow gap with a width of B_g=0.05 m between the two boxes, and the center of the narrow gap is always located at x=9.25 m. In this paper, only the piston-mode gap resonance is considered. For both boxes, their heights and drafts are kept identical and set to H=0.5 m and d=0.25 m, respectively. To consider different breadth ratios for the two boxes, the breadth of Box A, denoted by B_1, varies gradually from 0.2 m to 0.7 m, with an interval of 0.1 m; while the breadth of Box B, denoted by B_2, is kept unchanged and set to 0.5 m. Hence, the breadth ratio, defined as B_1/B_2, varies from 0.4 to 1.4. The still water depth is h=0.5 m.

In all numerical simulations, the incident regular waves with various frequencies and wave heights are produced at the inlet boundary of the flume. Six different incident wave heights (i.e., H_0 varying from 0.01 m to 0.06 m with an interval of 0.01 m) are considered. The incident wave frequency, f, ranges from 0.785 Hz to 0.979 Hz. Based on the linear dispersion relationship of water waves:

$$(2\pi f)^2 = \frac{2\pi g}{L}\tanh\left(\frac{2\pi h}{L}\right), \tag{3}$$

where the wavelength of the incident waves, L, ranges from 1.57 m to 2.24 m.

Six wave gauges (i.e., G_1−G_6) are arranged to record the time series of free water surface elevations at various locations. Based on the wave separation technique of Goda and Suzuki (1976), the wave height of the reflected waves from the two-box system can be calculated according to the time series of the free water surface elevations at G_1 and G_2. Subsequently, the reflection coefficient, C_R, defined as the ratio of the reflected wave height to the incident wave height, can be obtained. The distance between G_1 and G_2 and that between G_2 and the left edge of Box A are always set to 0.25 m and 2.0 m, respectively. G_4 is located at the middle of the gap. To record the wave climates around the two-box system, both G_3 and G_5 are placed very close to the upstream/downstream of the structure system with only the distance of 0.001 m from the edge of each box. G_6 is arranged at 2.0 m from the right edge of Box B to record the transmitted waves.

Two relaxation zones with a width of W_s=5.0 m each are arranged in the vicinity of both the inlet and outlet boundaries of the NWF to absorb the reflected and the transmitted waves. The length of 5.0 m is approximately 2.2 times the maximum wavelength that corresponds to the incident waves with f=0.785 Hz. Based on the research finding of Jacobsen et al. (2012) that the performance of the relaxation zone is already generally good when its width is equal to or larger than the incident wavelength, the setup of W_s=5.0 m in the present study ensures the perfect absorptions of both the reflected and the transmitted waves in the relaxation zones. For the convenience of the readers, all the parameters related to the setups of the NWF and the incident waves, and their physical meanings and magnitudes are further listed in Table 1.

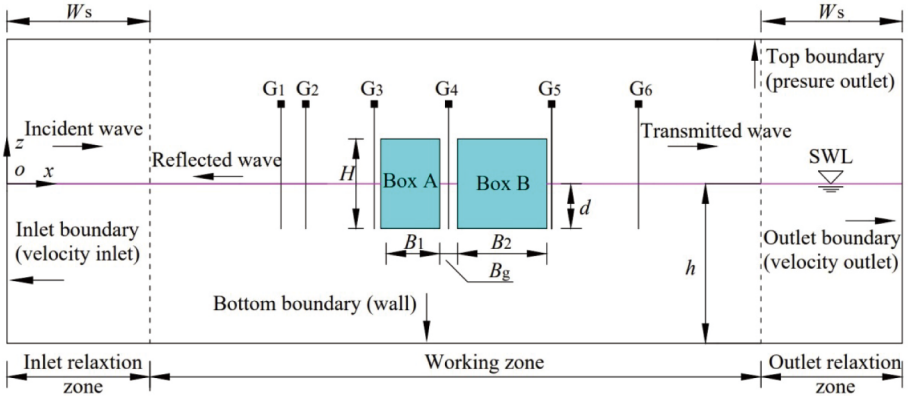

Fig. 1. Sketch of the NWF used in the present study.

Table 1 Physical meanings and magnitudes of all the parameters related to the setups of the NWF and incident regular waves

Parameter	Physical meaning	Magnitude
(o, x, y, z)	Cartesian coordinate system	–
B_1 (m)	Breadth of Box A	0.2, 0.3, 0.4, 0.5, 0.6, 0.7
B_2 (m)	Breadth of Box B	0.5
B_1/B_2	Breadth ratio of the two boxes	0.4, 0.6, 0.8, 1.0, 1.2, 1.4
B_g (m)	Width of the gap	0.05
d (m)	Draft of the box	0.25
f (Hz)	Incident wave frequency	0.785−0.979
f^*	Normalized incident wave frequency, defined as $f/(g/h)^{1/2}$	0.177−0.221
H (m)	Height of the box	0.5
H_0 (m)	Incident wave height	0.01, 0.02, 0.03, 0.04, 0.05, 0.06
h (m)	Water depth	0.5
L (m)	Incident wavelength	1.57−2.24
W_s (m)	Width of the relaxation zone	5.0

A mesh generation utility, "blockMesh", is adopted to discrete the computational domain and generate the meshes. A typical mesh configuration in the vicinity of the two-box system with the breadth ratio of B_1/B_2=0.6 is shown in Fig. 2. To reduce computational costs, non-uniform meshes are produced. Fine meshes with higher resolution are generated in the vicinity of the two-box system, especially within the narrow gap. To better capture the free water surface, the meshes become denser from the top/bottom boundaries of the NWF to the SWL.

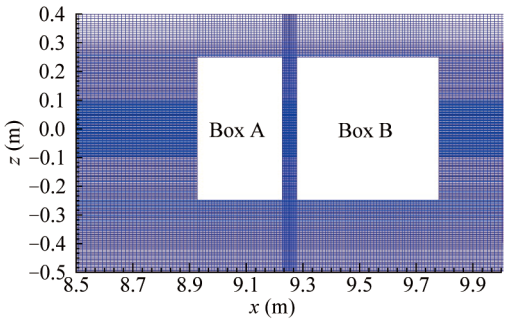

Fig. 2. Typical computational meshes in the vicinity of the two-box system (taking the case with the breadth ratio of B_1/B_2=0.6 as an example).

3.2 Analysis of mesh convergence

To examine the dependency of numerical results on mesh resolutions, the interactions between the incident waves and the two-box system with the breadth ratio of B_1/B_2=1.4 are simulated by using three meshes with various resolutions, namely Meshes 1–3. The details of the three meshes are listed in Table 2. The fluctuations of the free water surface elevations inside the gap for the incident waves with H_0=0.01 m and f^*= 0.177, 0.189 and 0.221 are shown in Fig. 3, where $A_0=H_0/2$ denotes the incident wave amplitude and $f^*= f/(g/h)^{1/2}$ is the normalized incident wave frequency. For Meshes 1 and 2, there exist slight differences between the time series of the free water surface elevations. However, for Meshes 2 and 3, the time series of the free water surface elevations become almost overlapping with each other. It indicates that the simulation results have reached convergence for Mesh 2. Hence, Mesh 2 is selected for all simulations.

For most cases, a total time of 40.0 s is simulated. However, to investigate the damping time of the resonant free water surface inside the gap, for the cases in which the incident wave frequency equates the resonant frequency of the fluid in the gap, a total time of 70.0 s is considered. The inlet boundary stops generating incident waves after 40.0 s, and the numerical model continues to simulate the damping process. It is seen from Fig. 3 that the time series of the free water surface elevation in the gap have already reached a steady state at t=20.0 s. All the results that will be shown in Subsections 4.1 and 4.2 are obtained based on the simulated steady-state data ranging from 20.0 s to 40.0 s. While in Subsection 4.3, the time series of the free wave surface elevation within the gap between 0–20.0 s and 40.0−70.0 s are respectively adopted to study the response time and the damping time of gap resonance.

3.3 Validation of the numerical model

To investigate the gap resonance phenomenon inside a narrow gap formed between two rectangular boxes with different breadths, Liu (2017) has performed a series of laboratory experiments in a physical wave flume. The setups of the laboratory experiments are similar to those shown in Fig. 1, overall. The physical wave flume is 50 m long and

Table 2 Details of Mesh 1, Mesh 2, and Mesh 3 for the two-box system with B_1/B_2=1.4

Name of mesh	No. of cells	No. of points	No. of faces	Sizes of cells across the gap (mm)	
				Δx	Δy
Mesh 1	101336	204870	406444	5.000	3.125
Mesh 2	204160	411450	818206	3.125	2.500
Mesh 3	408496	821406	1636192	2.500	1.563

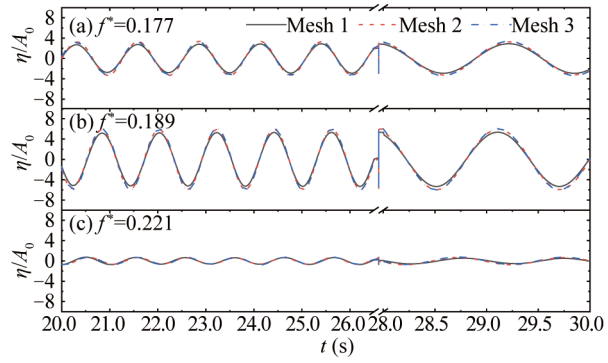

Fig. 3. Mesh dependence tests for the free surface elevation inside the gap for the structure system with B_1/B_2=1.4 suffered from the incident waves with H_0=0.01 m and (a) f^*= 0.177, (b) f^*= 0.189 and (c) f^*= 0.221.

0.8 m wide, with a constant water depth of h=0.5 m. Linear regular waves were generated by a piston wave maker. The incident wave height was set to H_0=0.03 m. A sloping beach covered with spongy materials was installed at the other end of the wave flume to eliminate transmitted waves. Two boxes with the same draft of d=0.25 m were firmly fixed in the wave flume. The upstream box (i.e., Box A) had a breadth of B_1=0.4 m, while the breadth of the downstream one (i.e., Box B) was B_2=0.8 m. A narrow gap with a width of B_g=0.05 m between them was formed.

Fig. 4 presents the amplification factors of the free water surface elevations in the narrow gap (i.e., H_g/H_0) subjected to the incident waves with various frequencies. H_g in the figure denotes the wave height inside the gap. It is seen that the resonant frequency of the fluid in the gap predicted by the present numerical model is almost identical to that obtained by the laboratory experiments. Moreover, for all the incident wave frequencies considered, the magnitudes of H_g/H_0 predicted by the numerical model also agree well with those obtained by the experiments.

4 Results and discussion

To present an overall impression on the gap resonance features of the two-box system with various breadth ratios,

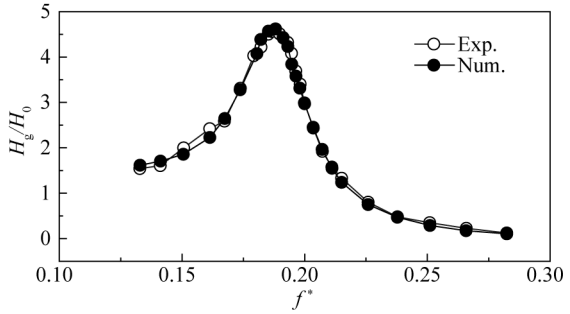

Fig. 4. Amplification factors of the wave height inside the narrow gap for the two-box system with B_1=0.4 m and B_2=0.8 m and for the incident waves with H_0=0.03 m and various frequencies. H_g in the figure denotes the wave height inside the gap.

the amplification factors of the wave heights both inside the gap and in the vicinity of the two-box system are first presented and studied in Subsection 4.1. Then, the reflection, transmission and energy loss coefficients of the two-box system with various breadth ratios are discussed in Subsection 4.2. Finally, the effects of the breadth ratio on both the response time and the damping time of gap resonance are systematically investigated in Subsection 4.3.

4.1 Wave height amplification

Fig. 5 illustrates the tendencies of the amplification factor of the wave height inside the gap with respect to the incident wave frequency under various incident wave heights. Two phenomena can be easily observed. Firstly, the resonant frequency of the fluid inside the gap that corresponds to the maximum wave height amplification for a certain set of H_0 and B_1/B_2 is shown to gradually decrease with the increase of B_1/B_2, no matter whether the incident wave height is large or small. To show this phenomenon more visually, Fig. 6 further presents the variation of the normalized resonant frequency of the fluid inside the gap [denoted by $(f^*)_{Hg}$ hereafter] with respect to the breadth ratio, B_1/B_2. Overall, the trend that the former gradually decreases with the latter is well reflected in Fig. 6, although there are some fluctuations in this downward trend. This phenomenon can be qualitatively explained as follows. According to Tan et al. (2017), the natural frequency of the fluid in the gap, $f_T{}^*$, for a structural system consisting of two fixed boxes with an identical draft can be theoretically expressed as:

$$f_T^* = \frac{1}{2\pi}\sqrt{\frac{h}{d+\dfrac{B^* B_g}{4(h-d)}}}, \tag{4}$$

where B^* represents the characteristic breadth of the two-box system, which linearly increases with the rise of the total breadth of the two-box system, B_1+B_2. In this study, B_2, B_g, h and d are kept fixed. Hence, as the value of B_1 increases, B^* increases correspondingly, which would naturally cause the decrease of the resonant frequency of the fluid inside the gap based on the above equation.

Secondly, it can also be seen from Fig. 5 that for all the incident wave heights considered, the amplification factor of the resonant wave height for a certain set of H_0 and B_1/B_2 [denoted by $(H_g/H_0)_{max}$ hereafter] decreases gradually with the rise of B_1/B_2 as well. The variations of $(H_g/H_0)_{max}$ with the breadth ratio under all the six incident wave heights are comprehensively illustrated in Fig. 7. It is seen that within the variation ranges of both the breadth ratio and the incident wave height, the magnitude of $(H_g/H_0)_{max}$ shows a linear downward trend with the breadth ratio overall. The reason why the downward trend is presented can be qualitatively explained as follows. As the value of B_2 remains unchanged in the present study, the larger value of B_1/B_2 means that the value of B_1 becomes larger. Based on the existing knowledge

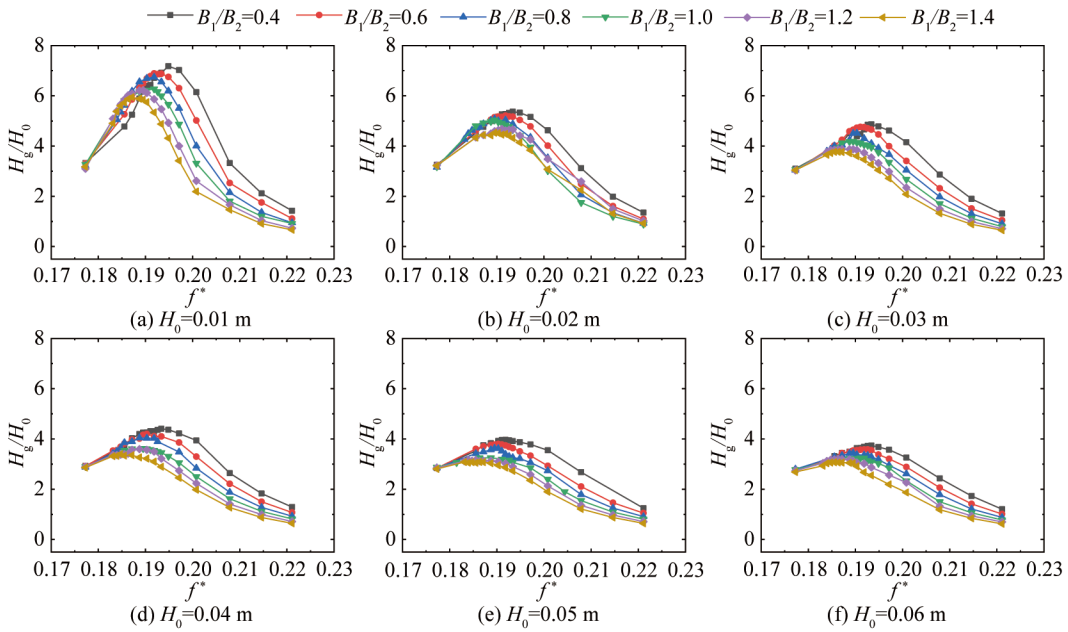

Fig. 5. Amplification factors of the wave height inside the gap excited by the incident waves with various wave heights and frequencies.

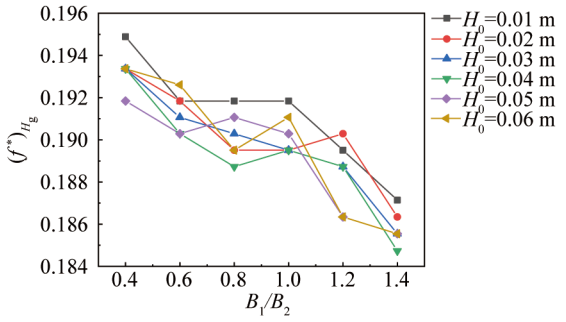

Fig. 6. Variations of the normalized resonant frequency of the fluid inside the gap with respect to the breadth ratio, B_1/B_2.

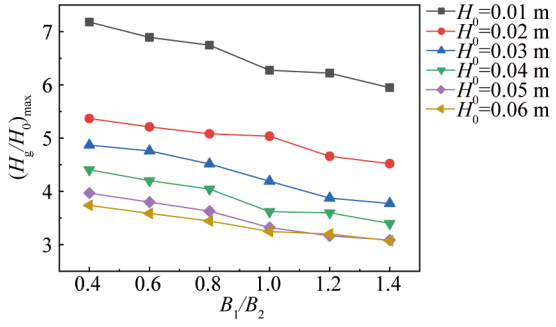

Fig. 7. Variations of the amplification factor of the resonant wave height for a certain set of H_0 and B_1/B_2, $(H_g/H_0)_{max}$, with respect to the breadth ratio under all the incident wave heights considered.

of floating breakwaters that a larger breakwater breadth can bring about a better sheltering effect on the incident waves (He et al., 2019; Ji et al., 2017; Nikpour et al., 2019), a wider upstream box (i.e., Box A) will reflect more incident wave energy, resulting in a smaller proportion of incident wave energy being transmitted into the narrow gap.

Besides the free water surface elevation inside the gap that is measured by gauge G_4, the wave climates both in front and at the rear of the two-box system are also recorded by gauges G_3 and G_5 in all simulations. Fig. 8 compares the amplification factors of the wave heights at these three locations under the condition of H_0=0.06 m. Three obvious phenomena are observed from this figure. Firstly, due to the sheltering effect of both boxes, the wave height at the rear of the structure system (i.e., H_b) is always significantly lower than those in front of the structure system and inside the gap within the range of the wave frequency considered, and the former monotonically decreases with the increase of the incident wave frequency.

Secondly, the relative size of H_f and H_g depends on the incident wave frequency. From the viewpoint of the green water on the deck, it indicates that the most dangerous position is not always located inside the gap. Instead, it depends on the incident wave frequency. Specifically, near the fluid resonant frequency $(f^*)_{Hg}$, the wave height inside the gap (i.e., H_g) is shown to be notably larger than that in front of the two-box system (i.e., H_f), regardless of the breadth ratio. However, as the incident wave frequency increases, H_g sharply decreases, but H_f only undergoes minor changes. At a certain frequency [denoted by $(f^*)_{IS}$], H_g starts to become lower than H_f. It implies that when the normalized incident wave frequency becomes larger than $(f^*)_{IS}$, the most dangerous position for the green water would shift from inside the gap to the front of the structure system.

Thirdly, although the magnitude of $(f^*)_{IS}$ is always larger than that of the corresponding $(f^*)_{Hg}$ for all the breadth ratios considered, both the former and the difference between them (i.e., $\triangle f^*$) are shown to gradually decrease with the

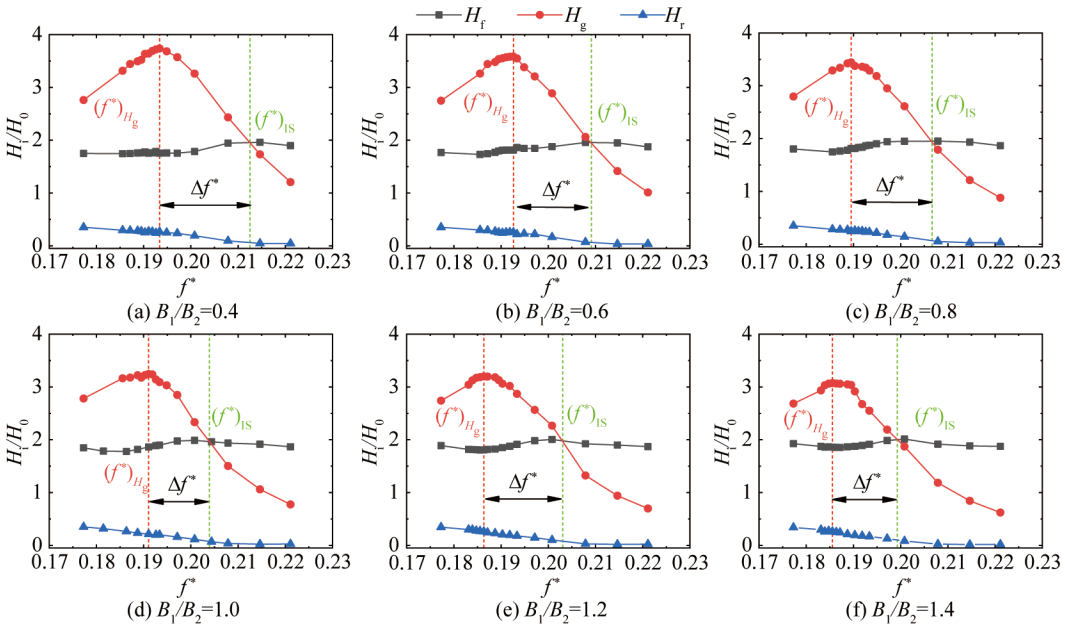

Fig. 8. Comparison of the amplification factors of the wave heights inside the gap, in front and at the rear of the structure system under the condition of H_0=0.06 m. H_f and H_b denote the wave height in front and at the rear of the structure system, respectively. The symbol "H_i" represents H_g, H_f or H_b. $(f^*)_{IS}$ denote the frequency where the two curves of H_g and H_f intersect with each other. $\triangle f^* = (f^*)_{IS} - (f^*)_{Hg}$.

increase of the breadth ratio. To present this phenomenon more comprehensively, Fig. 9 illustrates the variations of both $(f^*)_{IS}$ and $\triangle f^*$ with the breadth ratio for all the incident wave heights. It is shown that the downward trends of both $(f^*)_{IS}$ and $\triangle f^*$ with the breadth ratio appear not only for H_0= 0.06 m but also for all the other five wave heights. This indicates that for a structure system with a larger breadth ratio, the most dangerous position of green water is more likely to shift between inside the gap and in front of the structure system.

4.2 Reflection, transmission and energy loss coefficients

As mentioned in Subsection 3.1, the reflection coefficient, C_R, is defined as the ratio of the reflected wave height from the structure system to the incident wave height, H_0. The transmission coefficient, C_T, is defined as the ratio of the transmitted wave height to H_0. Subsequently, the energy loss coefficient that is defined as $L_E=1-C_R^2-C_T^2$ can be determined.

Fig. 10 presents the variations of both the reflection coefficient and the transmission coefficient with the wave frequency under various breadth ratios and H_0=0.01 m, 0.03 m and 0.05 m. It is seen that for C_R and C_T, their changing trends with the wave frequency are quite different. For C_R, it always first decreases and then increases with the increase of the wave frequency, regardless of the breadth ratio and the incident wave height. There always exists a minimum value, denoted by $(C_R)_{min}$ hereafter, near the resonant frequency of the fluid inside the gap. On the contrary, the tendency of C_T is found to rely on the incident wave height.

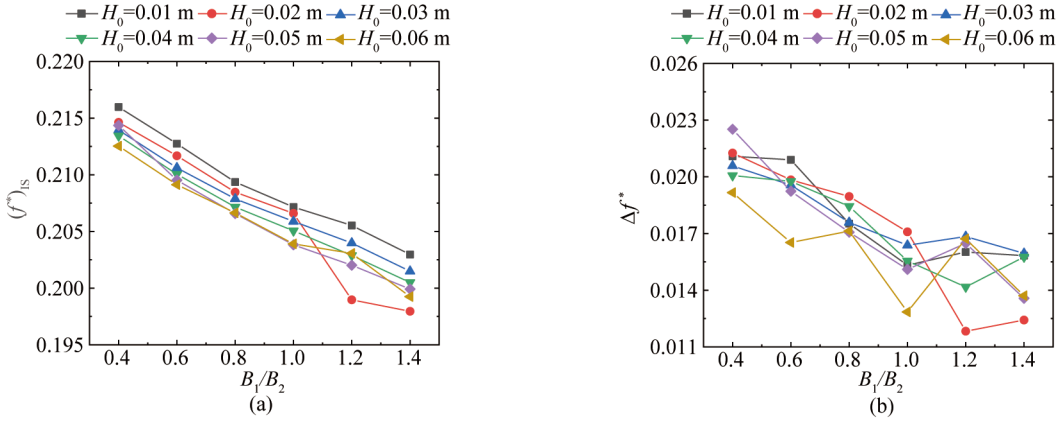

Fig. 9. Variations of $(f^*)_{IS}$ and $\triangle f^*$ with respect to the breadth ratio for all the incident wave heights considered. (a) and (b) correspond to $(f^*)_{IS}$ and $\triangle f^*$, respectively.

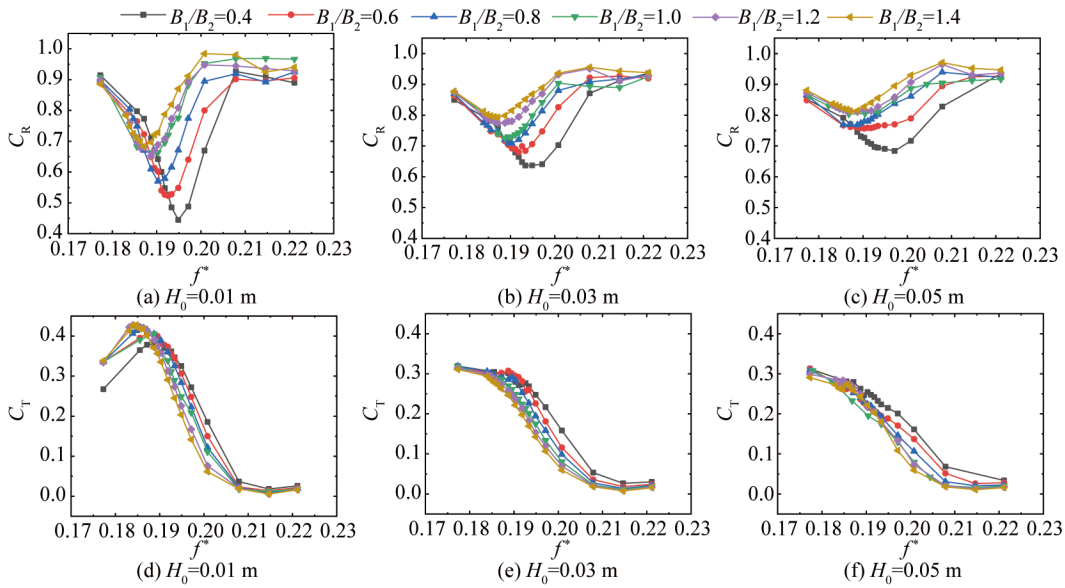

Fig. 10. Variations of (a–c) the reflection coefficient, C_R, and (d–f) the transmission coefficient, C_T, with the wave frequency under various breadth ratios and H_0=0.01 m, 0.03 m and 0.05 m.

For the lowest incident wave height considered (i.e., H_0= 0.01 m, see Fig. 10d), the value of C_T is found to first sharply increase, then sharply decrease, and then slowly increase with the increase of the incident wave frequency. However, as the incident wave height rises, C_T tends to become monotonically decreasing with the wave frequency (see Figs. 10e and 10f).

The changing trends of the minimum reflection coefficient for a certain set of H_0 and B_1/B_2, $(C_R)_{min}$, with respect to the breadth ratio under various incident wave heights are further illustrated in Fig. 11. It is seen that $(C_R)_{min}$ increases monotonically with the rise of the breadth ratio. It can be qualitatively explained as follows. For the current setups of the two-box system, the increase of the breadth ratio means the increase of the total breadth of the two-box system that includes the breadths of the two boxes and the width of the gap. If the two-box system was viewed as a floating breakwater, a larger breakwater breadth would result in a greater reflection of the incident waves (He et al., 2019; Ji et al., 2017; Nikpour et al., 2019).

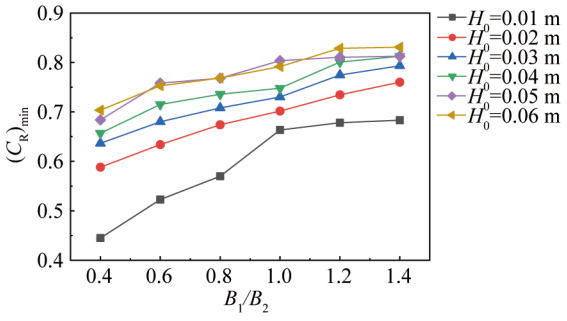

Fig. 11. Tendencies of the minimum reflection coefficient, $(C_R)_{min}$, with the breadth ratio.

Fig. 12 illustrates the variations of the energy loss coefficient, L_E, with the wave frequency under various breadth ratios and incident wave heights. In general, for each set of B_1/B_2 and H_0, the energy loss coefficient first monotonically increases and then gradually decreases as the incident wave frequency increases. For all sets of the incident wave height and the breadth ratio considered in this article, there always exists a maximum energy loss coefficient, denoted by $(L_E)_{max}$, at or near the fluid resonant frequency. Furthermore, the maximum energy loss coefficient is found to decrease gradually with the breadth ratio, which is further presented in Fig. 13 more comprehensively. It can be attributed to the fact that a larger breadth ratio causes a smaller amplification factor of the resonant wave height inside the gap (see Fig. 7), which would generate a lower intensity of vortices and vortex shedding in the vicinity of the narrow gap.

To verify the correctness of the above explanation, both vorticity and velocity fields around the narrow gap in the three cases with H_0=0.01 m and B_1/B_2=0.4, 0.8 and 1.4 are demonstrated in Fig. 14. The incident wave frequencies in the three cases are f^* =0.195, 0.192 and 0.187, which correspond respectively to the gap resonance frequencies of the structure systems with B_1/B_2=0.4, 0.8 and 1.4 subjected to the incident waves with H_0=0.01 m. In this figure, t_0 and t_0+ $T/4$ correspond to the time instant when the free water surface in the gap locates at the SWL (i.e., η=0) and the time instant when the free water surface in the gap reaches the highest elevation, respectively; t_0+2$T/4$ and t_0+3$T/4$ correspond to the time instant when the free water surface falls back to the SWL and the time instant when the free water surface reaches the lowest elevation, respectively. It can be visually observed from this figure that within a complete wave period, both the intensities of vortices and vortex shedding

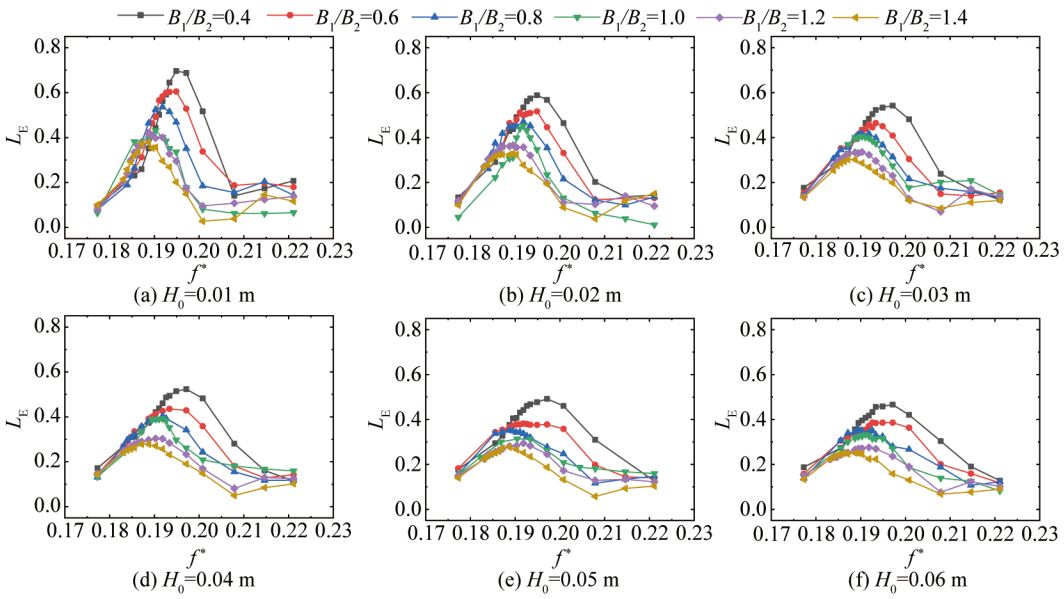

Fig. 12. Variations of the energy loss coefficient, L_E, with the wave frequency under various breadth ratios and incident wave heights.

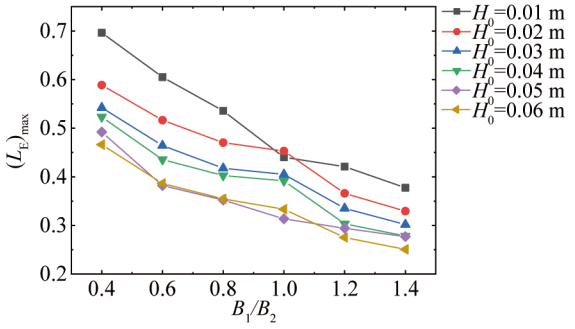

Fig. 13. Variations of the maximum energy loss coefficient, $(L_E)_{max}$, with the breadth ratio.

around the gap are shown to gradually decrease with the increase of the breadth ratio, overall.

4.3 Response time and damping time

In real engineering applications, the exact predictions of the response/damping time of gap resonance are crucial for the reasonable scheduling of loading/offloading operations and the safe evacuation of staffs. Therefore, the influences of the breadth ratio on both the response time and damping time for the steady-state gap resonance induced by regular waves are studied in this subsection.

A methodology for quantitatively assessing both the response time and the damping time of the steady-state gap resonance triggered by regular waves has been proposed in Gao et al. (2019b). For the response stage of the resonant fluid in the gap, the evolution of the free water surface elevation with the time can be expressed as:

$$\eta = \eta_{\max}\cos\left(-2\pi f_{H_g} t^*\right)\left(1-\mathrm{e}^{-\zeta^{\mathrm{R}} t^*}\right), \tag{5}$$

where ζ^{R} is a parameter determining the response time of the resonant fluid, $\eta_{\max}$ is the maximum response amplitude, $f_{Hg} = (f^*)_{Hg}\times(g/h)^{1/2}$ denotes the dimensional resonant frequency of the fluid in the gap, and t^* refers to the relative time with respect to the moment that the free surface elevation just starts to move from the rest. According to Eq. (5), the free surface oscillation needs infinite time to achieve its maximum. The time length, $t^*_{\alpha\%}$, required for the oscillation to achieve α% of its maximum can be further expressed as:

$$t^*_{\alpha\%} = -\frac{\ln(1-\alpha\%)}{\zeta^{\mathrm{R}}}. \tag{6}$$

Similarly, if the resonant fluid decays from its steady-state maximum to the rest, the free surface elevation can be expressed as:

$$\eta = \eta_{\max}\cos\left(-2\pi f_{H_g}\tau\right)\mathrm{e}^{-\zeta^{\mathrm{D}}\tau}, \tag{7}$$

in which ζ^{D} is a parameter determining the damping time of the resonant fluid, and τ refers to the relative time with respect to the moment that the fluid just starts to decay from its steady-state maximum. The time length, τ_β , required for the oscillation to decrease to β% of the maximum can be further formulated as:

$$\tau_{\beta\%} = -\frac{\ln(\beta\%)}{\zeta^{\mathrm{D}}}. \tag{8}$$

As in Gao et al. (2020a, 2019b), $t^*_{95\%}$ and τ_5 are respectively chosen to represent the response time and the damping time of the resonant fluid in this article.

Fig. 15 presents the time series of the simulated free water surface elevations inside the gap from the calm to the steady state and their corresponding fitted envelopes by Eq. (5). The incident wave frequency in each case corresponds to the resonant frequency of the fluid in the gap. Via fitting the simulated envelope with the theoretical one expressed

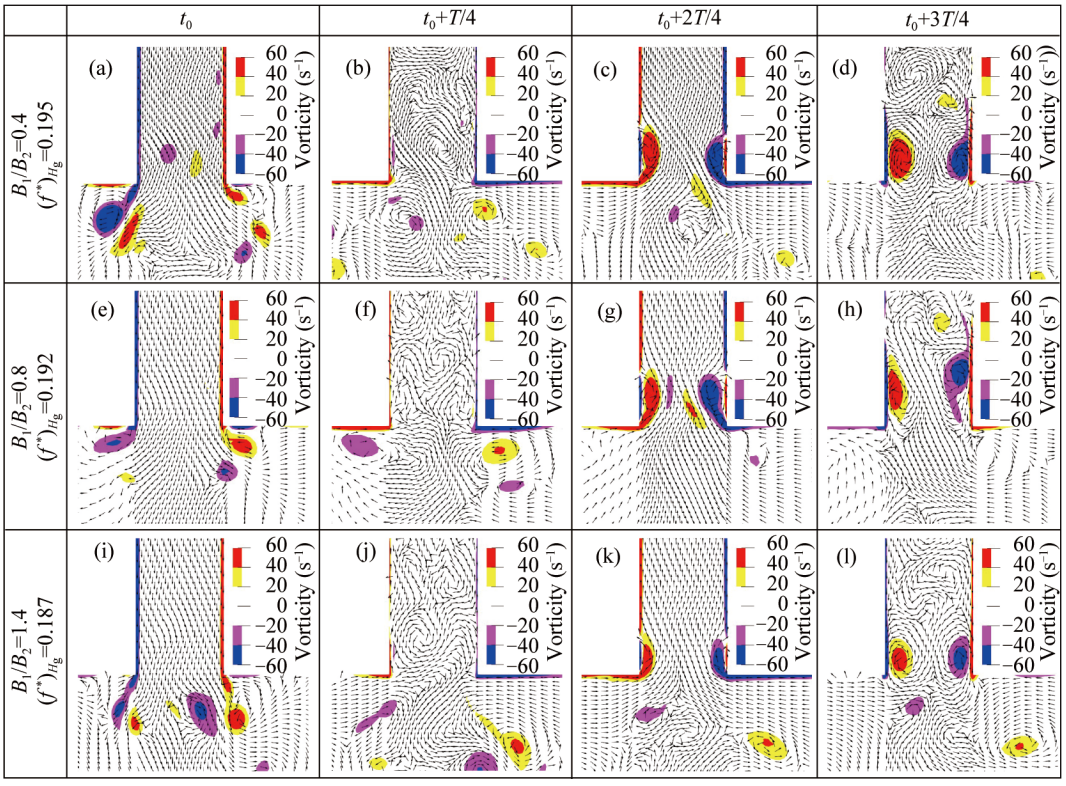

Fig. 14. Vorticity and velocity fields during one period of gap resonance with T/4 interval for the structure system with B_1/B_2=0.4, 0.8 and 1.4 subjected to the waves with H_0=0.01 m.

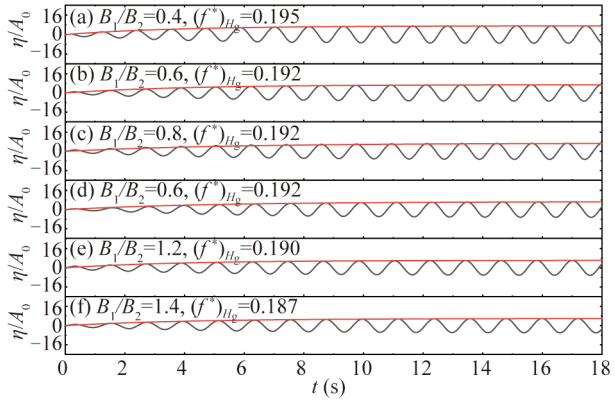

Fig. 15. Response stage of the free wave surface elevation (η/A_0) in the narrow gap excited by incident waves with H_0=0.01 m and the frequencies corresponding to the resonant frequencies of the fluid in the gap. Black lines are the time series of the simulated free water surface elevations. Red lines are the fitted envelopes of η/A_0 via directly fitting the simulated envelopes with the theoretical ones expressed by Eq. (5).

by Eq. (5), the values of both ζ^R and $t^*_{95\%}$ can be determined, and their specific values for the six cases shown in the figure are listed in Table 3. Via observing Fig. 15, it is easily found that for all the breadth ratios considered, the fitted envelopes of the free water surface elevations are well in coincidence with the corresponding simulated ones, which indicates that Eq. (5) is accurate and reliable in evaluating the response time of the steady-state gap resonance.

Fig. 16 comprehensively presents the variations of the response time, $t^*_{95\%}$, with respect to the breadth ratio, B_1/B_2, under the condition of the occurrence of gap resonance for all the incident wave heights. In general, the response time of gap resonance is shown to first gradually increase and then gradually decrease with the rise of the breadth ratio, no matter whether the incident wave height is large or small. The maximum value of the response time always appears at B_1/B_2=1.0. That is, the two boxes with the same breadth will bring the largest response time of gap resonance.

Table 3 All the parameters related to the response time and the damping time of the resonant free water surface elevations in the gap shown in Figs. 15 and 17

Cases		ζ^R	$t^*_{95\%}$ (s)	ζ^D	$\tau_{5\%}$ (s)
B_1/B_2	$(f^*)_{Hg}$				
0.4	0.195	0.265	11.32	0.143	20.96
0.6	0.192	0.255	11.77	0.136	22.01
0.8	0.192	0.243	12.31	0.127	23.60
1.0	0.192	0.201	14.88	0.123	24.36
1.2	0.190	0.260	11.50	0.128	23.38
1.4	0.187	0.241	12.41	0.128	23.45

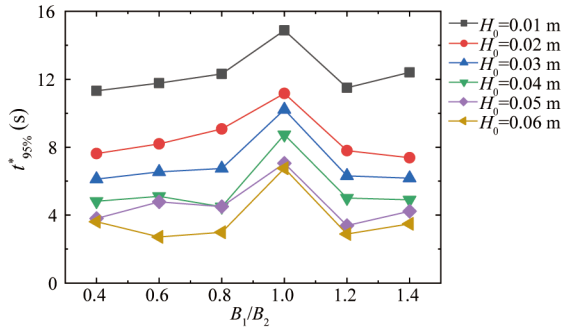

Fig. 16. Variations of the response time with the breadth ratio under the condition of the occurrence of gap resonance for all the incident wave heights. The incident wave frequencies for all these cases are comprehensively presented in Fig. 6.

Fig. 17 demonstrates the time series of the simulated free water surface elevations within the gap and their fitted envelopes obtained by fitting the simulated envelopes with the theoretical ones formulated by Eq. (7) during the damping stage. Like Fig. 15, it can be observed from Fig. 17 that for all the breadth ratios considered, Eq. (7) well depicts the attenuation trend of the resonant free water surface elevation inside the gap. The specific magnitudes of both ζ^{D} and the damping time, τ_5 , obtained by fitting the envelope of free water surface oscillations under various breadth ratios are also listed in Table 3.

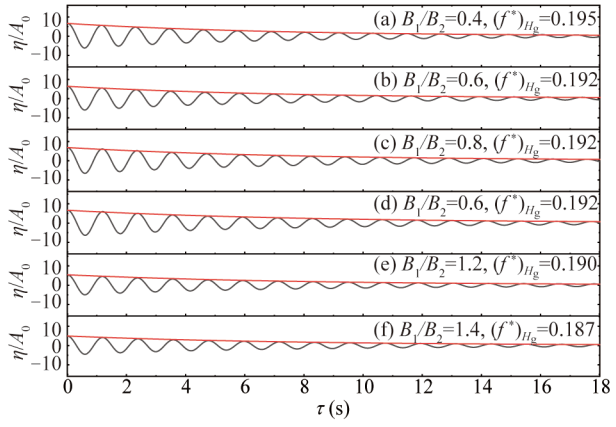

Fig. 17. Similar to Fig. 15, but for the damping stage of the free water surface elevation in the gap. Black lines are the time series of the simulated free water surface elevations. Red lines are the fitted envelopes of η/A_0 via fitting the simulated envelopes with the theoretical ones expressed by Eq. (7).

The variations of the damping time, $\tau_{5\%}$, with respect to the breadth ratio under the condition of the occurrence of gap resonance for all the incident wave heights are further presented in Fig. 18. Unlike the response time, the changing trends of the damping time of gap resonance with the breadth ratio are shown to depend heavily on the incident wave height. For H_0=0.01 m and 0.05 m, the damping time is shown to first increase and then decrease with the breadth ratio, and there exists a maximum value at B_1/B_2=1.0. However, for the other four wave heights, the damping time seems to fluctuate around specific constant values within the range of the breadth ratio considered.

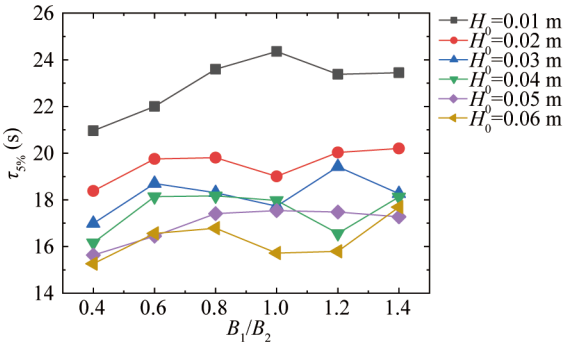

Fig. 18. Variations of the damping time, $\tau_{5\%}$, with the breadth ratio under the condition of the occurrence of gap resonance for all the incident wave heights. The incident wave frequencies for all these cases are comprehensively presented in Fig. 6.

5 Conclusions

In this article, the open-sourced CFD package OpenFOAM, together with the toolbox "waves2Foam", is utilized to study the fluid resonance phenomenon inside a narrow gap formed by two stationary boxes. Gap resonance is excited by the incident regular waves with various frequencies and wave heights. The two boxes have identical draft and height. The breadth of the upstream box, B_1, varies from 0.2 m to 0.7 m, and the breadth of the downstream box is kept as a constant of B_2 = 0.5 m for all simulations. Hence, the breadth ratio, defined as B_1/B_2, varies from 0.4 to 1.4. The influences of the breadth ratio on the following three aspects of hydrodynamic characteristics of gap resonance are investigated in detail: (1) the wave height amplifications inside the gap, and in front and at the rear of the structure system, (2) the reflection, transmission, and energy loss coefficients of the structure system, and (3) the response and damping time of the fluid resonance. The results of this paper have provided new insights into the hydrodynamic features of gap resonance. The following conclusions can be drawn.

(1) The resonant frequency of the fluid inside the gap is found to gradually decrease with the increase of the breadth ratio, B_1/B_2, although there are some fluctuations in this downward trend. Similarly, the amplification factor of the resonant wave height inside the gap, $(H_g/H_0)_{\max}$, shows a linear downward trend with the breadth ratio under all the incident wave heights considered.

(2) From the viewpoint of the green water on the deck, the most dangerous position is not always located inside the gap. Instead, it depends on the incident wave frequency. When the incident wave frequency is near the fluid resonant frequency, the most dangerous position indeed locates inside the gap, regardless of the breadth ratio. However, as the incident wave frequency increases, the most dangerous

position shifts from inside the gap to the front of the structure system. Furthermore, a larger breadth ratio would bring a greater likelihood for the shift of the most dangerous position between in the gap and in front of the structure system.

(3) The changing trends of the reflection coefficient and the energy loss coefficient with respect to the wave frequency are quite different. The reflection coefficient always first decreases and then increases with the wave frequency. Its minimum value, $(C_R)_{min}$, increases monotonically with the breadth ratio. Exactly opposite to the reflection coefficient, the energy loss coefficient first increases and then decreases with the wave frequency. The maximum energy loss coefficient, $(L_E)_{max}$, decreases monotonically with the breadth ratio. The tendency of the transmission coefficient with the breadth ratio is found to rely on the incident wave height.

(4) In general, the response time of gap resonance is shown to first gradually increase and then gradually decrease with the breadth ratio, regardless of the incident wave height. The configuration that the two boxes have the same breadth would bring the largest response time of gap resonance. The changing trends of the damping time of gap resonance with the breadth ratio are found to depend heavily on the incident wave height.

Finally, we affirm here that these conclusions are only valid for the given geometric layout (including the height and draft of the two boxes, the gap width and the water depth) and the variation ranges of the breadth ratio, the incident wave height and the incident wave frequency adopted in this article.

Competing interests

The authors declare no competing interests.

References

Chen, L.F., Zang, J., Hillis, A.J., Morgan, G.C.J. and Plummer, A.R., 2014. Numerical investigation of wave-structure interaction using OpenFOAM, *Ocean Engineering*, 88, 91–109.

Chen, M.S., Guo, H.R., Wang, R., Tao, R. and Cheng, N., 2021. Effects of gap resonance on the hydrodynamics and dynamics of a multi-module floating system with narrow gaps, *Journal of Marine Science and Engineering*, 9(11), 1256.

Ding, Y.F., Walther, J.H. and Shao, Y.L., 2022a. Higher-order gap resonance and heave response of two side-by-side barges under Stokes and cnoidal waves, *Ocean Engineering*, 266, 112835.

Ding, Y.F., Walther, J.H. and Shao, Y.L., 2022b. Higher-order gap resonance between two identical fixed barges: A study on the effect of water depth, *Physics of Fluids*, 34(5), 052113.

Ekerhovd, I., Ong, M.C., Taylor, P.H. and Zhao, W.H., 2021. Numerical study on gap resonance coupled to vessel motions relevant to side-by-side offloading, *Ocean Engineering*, 241, 110045.

Feng, X., Bai, W., Chen, X.B., Qian, L. and Ma, Z.H., 2017. Numerical investigation of viscous effects on the gap resonance between side-by-side barges, *Ocean Engineering*, 145, 44–58.

Gao, J.L., Bi, W.J., Zhang, J. and Zang, J., 2023a. Numerical investigations on harbor oscillations induced by falling objects, *China Ocean Engineering*, 37(3), 458–470.

Gao, J.L., Chen, H.Z., Zang, J., Chen, L.F., Wang, G. and Zhu, Y.Z., 2020a. Numerical investigations of gap resonance excited by focused transient wave groups, *Ocean Engineering*, 212, 107628.

Gao, J.L., Gong, S.K., He, Z.W., Shi, H.B., Zang, J., Zou, T. and Bai, X., 2023b. Study on wave loads during steady-state gap resonance with free heave motion of floating structure, *Journal of Marine Science and Engineering*, 11(2), 448.

Gao, J.L., He, Z.W., Huang, X.H., Liu, Q., Zang, J. and Wang, G., 2021. Effects of free heave motion on wave resonance inside a narrow gap between two boxes under wave actions, *Ocean Engineering*, 224, 108753.

Gao, J.L., He, Z.W., Zang, J., Chen, Q., Ding, H.Y. and Wang, G., 2019a. Topographic effects on wave resonance in the narrow gap between fixed box and vertical wall, *Ocean Engineering*, 180, 97–107.

Gao, J.L., He, Z.W., Zang, J., Chen, Q., Ding, H.Y. and Wang, G., 2020b. Numerical investigations of wave loads on fixed box in front of vertical wall with a narrow gap under wave actions, *Ocean Engineering*, 206, 107323.

Gao, J.L., Lyu, J., Wang, J.H., Zhang, J., Liu, Q., Zang, J. and Zou, T., 2022a. Study on transient gap resonance with consideration of the motion of floating body, *China Ocean Engineering*, 36(6), 994–1006.

Gao, J.L., Lyu, J., Zhang, J. and Zang, J., 2023c. Influences of floater motion on gap resonance triggered by focused wave groups, *China Ocean Engineering*, 37(4), 685–697.

Gao, J.L., Zang, J., Chen, L.F., Chen, Q., Ding, H.Y. and Liu, Y.Y., 2019b. On hydrodynamic characteristics of gap resonance between two fixed bodies in close proximity, *Ocean Engineering*, 173, 28–44.

Gao, S., Cong, P.W. and Teng, B., 2022b. Effect of incident wave angle to gap resonance between two fixed barges, *Ocean Engineering*, 257, 111583.

Goda, Y. and Suzuki, T., 1976. Estimation of incident and reflected waves in random wave experiments, *Proceedings of the 15th Coastal Engineering Conference*, ASCE, Honolulu, Hawaii, pp. 828–845.

He, M., Gao, X.F., Xu, W.H., Ren, B. and Wang, H.S., 2019. Potential application of submerged horizontal plate as a wave energy breakwater: A 2D study using the WCSPH method, *Ocean Engineering*, 185, 27–46.

He, Z.W., Gao, J.L., Chen, H.Z., Zang, J., Liu, Q. and Wang, G., 2021a. Harmonic analyses of hydrodynamic characteristics for gap resonance between fixed box and vertical wall, *China Ocean Engineering*, 35(5), 712–723.

He, Z.W., Gao, J.L., Shi, H.B., Zang, J., Chen, H.Z. and Liu, Q., 2022. Investigation on effects of vertical degree of freedom on gap resonance between two side-by-side boxes under wave actions, *China Ocean Engineering*, 36(3), 403–412.

He, Z.W., Gao, J.L., Zang, J., Chen, H.Z., Liu, Q. and Wang, G., 2021b. Effects of free heave motion on wave forces on two side-by-side boxes in close proximity under wave actions, *China Ocean Engineering*, 35(4), 490–503.

Jacobsen, N.G., Fuhrman, D.R. and Fredsøe, J., 2012. A wave generation toolbox for the open-source CFD library: OpenFoam®, *International Journal for Numerical Methods in Fluids*, 70(9), 1073–1088.

Ji, C.Y., Cheng, Y., Yang, K. and Oleg, G., 2017. Numerical and experimental investigation of hydrodynamic performance of a cylindrical dual pontoon-net floating breakwater, *Coastal Engineering*, 129, 1–16.

Jiang, S.C., Bai, W. and Yan, B., 2021. Higher-order harmonic

induced wave resonance for two side-by-side boxes in close proximity, *Physics of Fluids*, 33(10), 102113.

Jiang, S.C., Liu, H., Sun, T.Z. and Gu, Q., 2020. Numerical simulation for hydrodynamic behavior of box-systems with and without narrow gaps, *Ocean Engineering*, 214, 107698.

Jin, R.J., Teng, B., Ning, D.Z., Zhao, M. and Cheng, L., 2017. Numerical investigation of influence of wave directionality on the water resonance at a narrow gap between two rectangular barges, *Acta Oceanologica Sinica*, 36(6), 104–111.

Li, Y.J. and Zhang, C.W., 2016. Analysis of wave resonance in gap between two heaving barges, *Ocean Engineering*, 117, 210–220.

Li, Y.J., 2019. Fully nonlinear analysis of second-order gap resonance between two floating barges, *Engineering Analysis with Boundary Elements*, 106, 1–19.

Li, Z.Y., Hu, H.B., Wang, C., Xie, Z.L., Chen, X.P., Yuan, Z.M. and Du, P., 2024. Hydrodynamics and stability of oblique water entry in waves, *Ocean Engineering*, 292, 116506.

Liang, H., Chua, K.H., Wang, H.C. and Choo, Y.S., 2021. Numerical and experimental investigations into fluid resonance in a gap between two side-by-side vessels, *Applied Ocean Research*, 111, 102581.

Liang, H., Liu, X.B., Chua, K.H., de Mello, P.C. and Choo, Y.S., 2022. Wave actions on side-by-side barges with sloshing effects: fixed-free arrangement, *Flow*, 2, E20.

Liu, C.Y., 2017. *Experimental and Numerical Study of Hydrodynamic Responses of Side-By-Side Floating Bodies under Wave Action*, MSc. Thesis, Dalian University of Technology, Dalian. (in Chinese)

Liu, J.S., Gao, J.L., Shi, H.B., Zang, J. and Liu, Q., 2022. Investigations on the second-order transient gap resonance induced by focused wave groups, *Ocean Engineering*, 263, 112430.

Meringolo, D.D., Liu, Y. and Lu, L., 2018. Energy analysis of wave resonance in a gap through an SPH model, *Proceedings of the 28th International Ocean and Polar Engineering Conference*, ISOPE, Sapporo, Japan, pp. 338–344.

Miao, G.P., Saitoh, T. and Ishida, H., 2001. Water wave interaction of twin large scale caissons with a small gap between, *Coastal Engineering Journal*, 43(1), 39–58.

Molin, B., 2001. On the piston and sloshing modes in moonpools, *Journal of Fluid Mechanics*, 430, 27–50.

Nikpour, A.H., Moghim, M.N. and Badri, M.A., 2019. Experimental study of wave attenuation in trapezoidal floating breakwaters, *China Ocean Engineering*, 33(1), 103–113.

Ning, D.Z., Su, X.J., Zhao, M. and Teng, B., 2015a. Hydrodynamic difference of rectangular-box systems with and without narrow gaps, *Journal of Engineering Mechanics*, 141(8), 04015023.

Ning, D.Z., Su, X.J., Zhao, M. and Teng, B., 2015b. Numerical study of resonance induced by wave action on multiple rectangular boxes with narrow gaps, *Acta Oceanologica Sinica*, 34(5), 92–102.

Saitoh, T., Miao, G.P. and Ishida, H., 2006. Theoretical analysis on appearance condition of fluid resonance in a narrow gap between two modules of very large floating structure, *Proceedings of the 3rd Asia-Pacific Workshop on Marine Hydrodynamics*, Shanghai,China, 170–175.

Shivaji, G.T. and Sen, D., 2016. Time domain simulation of side-by-side floating bodies using a 3D numerical wave tank approach, *Applied Ocean Research*, 58, 189–217.

Song, Z.W., Lu, L., Li, C., Lou, X.F., Tang, G.Q. and Liu, Y., 2021. An effective resonant wave absorber for long regular water waves, *Applied Ocean Research*, 117, 102966.

Tan, L., Cheng, L. and Ikoma, T., 2021. Damping of piston mode resonance between two fixed boxes, *Physics of Fluids*, 33(6), 062117.

Tan, L., Lu, L., Liu, Y., Sabodas, O.A. and Teng, B., 2014. Dissipative effects of resonant waves in confined space formed by floating box in front of vertical wall, *Proceedings of the Eleventh ISOPE Pacific/Asia Offshore Mechanics Symposium*, ISOPE, Shanghai, China.

Tan, L., Lu, L., Tang, G.Q. and Cheng, L., 2020. A dynamic solution for predicting resonant frequency of piston mode fluid oscillation in moonpools/narrow gaps, *Journal of Hydrodynamics*, 32(1), 54–69.

Tan, L., Tang, G.Q., Zhou, Z.B., Cheng, L., Chen, X.B. and Lu, L., 2017. Theoretical and numerical investigations of wave resonance between two floating bodies in close proximity, *Journal of Hydrodynamics*, 29(5), 805–816.

Vineesh, P. and Sriram, V., 2021. Numerical investigation of wave actions on two side by side boxes in close proximity using IMLPG_R method, *Applied Ocean Research*, 116, 102892.

Vineesh, P. and Sriram, V., 2023. Numerical investigation of wave interaction with two closely spaced floating boxes using particle method, *Ocean Engineering*, 268, 113465.

Wang, H.C., Draper, S., Zhao, W.H., Wolgamot, H. and Cheng, L., 2018. Development of a computational fluid dynamics model to simulate three-dimensional gap resonance driven by surface waves, *Journal of Offshore Mechanics and Arctic Engineering*, 140, 061803.

Wang, X.Y., Liu, Y. and Lu, L., 2022. Three-dimensional (3D) semi-analytical solution of wave-induced fluid resonance in narrow gaps of caisson-type breakwaters, *Ocean Engineering*, 253, 111305.

Xie, C., Zhou, L., Ding, S.F., Liu, R.W. and Zheng, S.J., 2023. Experimental and numerical investigation on self-propulsion performance of polar merchant ship in brash ice channel, *Ocean Engineering*, 269, 113424.

Yin, Y., Jiang, S.C. and Geng, B.L., 2022. Fluid resonance in the narrow gap for a box close to a bottom-mounted wall with permeable bed, *Ocean Engineering*, 258, 111726.

Yin, Y., Jiang, S.C. and Liu, H., 2023. Fluid resonance in the narrow gap for a ship close to the vertical caisson on impermeable and permeable beds, *Ocean Engineering*, 286, 115422.

Zhang, C.W., Sun, X.T., Wang, P.F., Chen, L.F. and Ning, D.Z., 2022. Hydrodynamics of a floating liquid-tank barge adjacent to fixed structure in beam waves, *Physics of Fluids*, 34(4), 047114.

Zhao, W., Milne, I.A., Efthymiou, M., Wolgamot, H.A., Draper, S., Taylor, P.H. and Taylor, R.E., 2018. Current practice and research directions in hydrodynamics for FLNG-side-by-side offloading, *Ocean Engineering*, 158, 99–110.

Zhao, W., Wolgamot, H.A., Taylor, P.H. and Taylor, R.E., 2017. Gap resonance and higher harmonics driven by focused transient wave groups, *Journal of Fluid Mechanics*, 812, 905–939.

Zou, M.Y., Chen, M.S., Zhu, L., Li, L. and Zhao, W.H., 2023. A constant parameter time domain model for dynamic modelling of multi-body system with strong hydrodynamic interactions, *Ocean Engineering*, 268, 113376.